A Paired Phase and Magnitude Reconstruction for Advanced Diffusion-Weighted Imaging

Chen Qian, Zi Wang, Xinlin Zhang, Boxuan Shi, Boyu Jiang, Ran Tao, Jing Li, Yuwei Ge, Taishan Kang, Jianzhong Lin, Di Guo, and Xiaobo Qu*

Abstract*—*Objective: Multi-shot interleaved echo planer imaging (Ms-iEPI) can obtain diffusion-weighted images (DWI) with high spatial resolution and low distortion, but suffers from ghost artifacts introduced by phase variations between shots. In this work, we aim at solving the ms-iEPI DWI reconstructions under inter-shot motions and ultra-high b-values. ***Methods***: An iteratively joint estimation model with paired phase and magnitude priors is proposed to regularize the reconstruction (PAIR). The former prior is low-rankness in the k-space domain. The latter explores similar edges among multi-b-value and multi-direction DWI with weighted total variation in the image domain. The weighted total variation transfers edge information from the high SNR images (b-value=0) to DWI reconstructions, achieving simultaneously noise suppression and image edges preservation. ***Results***: Results on simulated and *in vivo* data show that PAIR can remove inter-shot motion artifacts very well (8 shots) and suppress the noise under the ultra-high b-value (4000 s/mm^2) significantly. ***Conclusion***: The joint estimation model PAIR with complementary priors has a good performance on challenging reconstructions under inter-shot motions and a low signal-to-noise ratio. ***Significance***: PAIR has potential in advanced clinical DWI applications and microstructure research.

***Index Terms*—multi-shot, DWI, high-resolution, ultra-high b-value, reconstruction.**

I. Introduction

DIFFUSION-WEIGHTED image (DWI) is a non-invasive tool for imaging water molecules diffusion [1]. It has been widely employed in the clinical diagnosis of acute stroke [2, 3] and cancer [4-6] and the scientific research of brain fiber tractography [7, 8]. To achieve high spatial resolution and low distortion DWI, multi-shot interleaved echo planer imaging has become increasingly popular [6, 9]. This imaging scheme samples different segments of k-space uniformly along phase encoding direction in different shots. However, during the data acquisition of each shot, subject or physiological motions are easily introduced, leading to strong phase variations of each shot image and finally producing ghosting image artifacts [10].

Phase variations can be corrected by navigator-based [10-13] and navigator-free methods [14-21]. The former requires extra navigator echo acquisition, and geometric mismatches between the navigator echo and target image echo need to be compensated [11, 13]. Navigator-free methods have been attached with increasing attention recently [14-21]. They can be classified into three categories: implicit phase [14-17], explicit phase [18, 22], and joint estimation of phase and magnitude [19-21].

Implicit phase reconstructions recover the image of each shot and then combine them into a magnitude image by the sum of squares (SOS) [14-17]. These approaches avoid the estimation of the phase of each shot image, i.e., the shot phase. Recently, inspired by models and priors in fast magnetic resonance imaging [23, 24], many state-of-the-art methods exploit low-rank properties in multi-shot interleaved echo planer imaging DWI. In MUSSELS [15], cross-shot annihilating filter relations deduced from smooth phase modulations are exploited, and the missing samples are interpolated from multi-shot data by a structured low-rank matrix completion formulation [15]. In PLRHM [17], intra-shot annihilating filter relations are employed for low-rank matrix construction.

Explicit phase methods have two steps. Firstly, they estimate the each shot phase from individual shot image using parallel imaging such as SENSE. Then, all shot data are incorporated to build an integrated reconstruction problem for estimation of magnitude image, assuming that different shot images share the same magnitude [18]. A representative explicit phase method is MUSE. Compared with implicit phase reconstruction, once the shot phase is estimated, the explicit phase strategy decreases the number of unknowns, which improves matrix inversion conditioning [18, 19]. This strategy can bring benefits in low signal-to-noise ratio (SNR) imaging scenarios, such as high b-value DWI [18].

However, an accurate phase estimation is not easy for explicit phase reconstruction. The step-by-step estimation of shot phase and magnitude in MUSE can hardly get reliable shot phases, when the shot number is high, say eight [15]. The low-

This work was supported in part by the National Natural Science Foundation of China (62122064, 61971361, and 61871341), the Natural Science Foundation of Fujian Province of China under grant (2021J011184), the President Fund of Xiamen University (20720220063), and the Xiamen University Nanqiang Outstanding Talents Program.

Chen Qian, Zi Wang, Xinlin Zhang, Boxuan Shi, and Xiaobo Qu* are with the Department of Electronic Science, Biomedical Intelligent Cloud R&D Center, Fujian Provincial Key Laboratory of Plasma and Magnetic Resonance, National Institute for Data Science in Health and Medicine, Xiamen University, Xiamen 361005, China (*Corresponding author, email: quxiaobo@xmu.edu.cn).

Boyu Jiang and Ran Tao are with the United Imaging Healthcare, Shanghai 201807, China.

Jing Li and Yuwei Ge are with Xingaoyi Medical Equipment Company Limited, Yuyao 315400, China.

Taishan Kang and Jianzhong Lin are with Department of Radiology, Zhongshan Hospital of Xiamen University, School of Medicine, Xiamen University, Xiamen 361006, China.

Di Guo is with the School of Computer and Information Engineering, Xiamen University of Technology, Xiamen 361024, China.

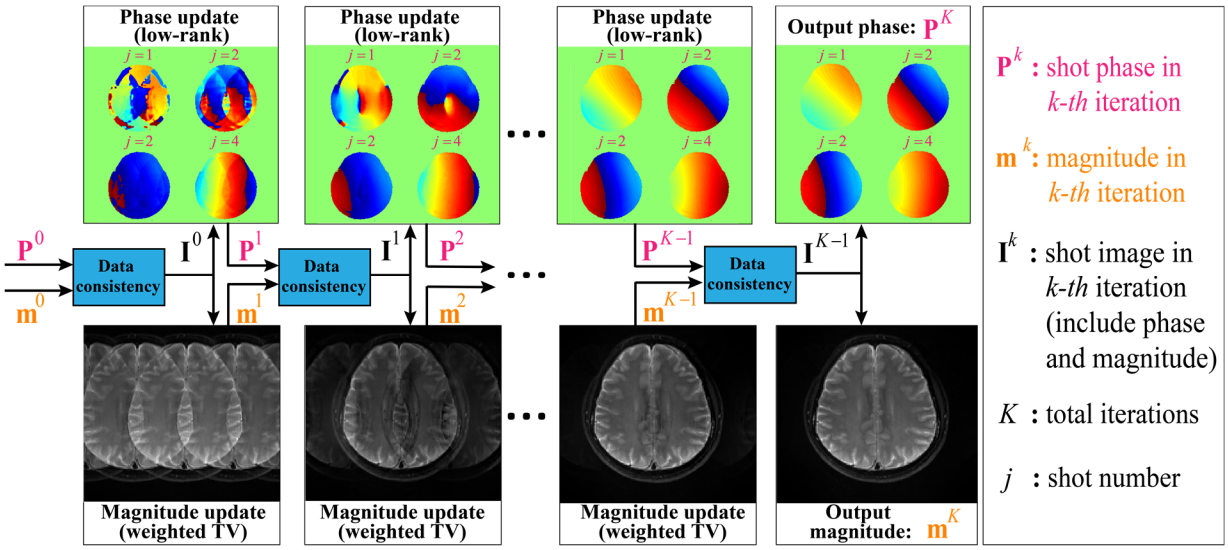

Fig. 1. Iteratively updated shot phase and magnitude images in PAIR. Low-rank and weighted total variation are used as a pair of complementary priors to facilitate phase and magnitude image reconstruction. Note: TV is short for total variation.

quality shot phases will decrease the final reconstruction performance.

The joint estimation methods [19-21] iteratively solve the shot phase and magnitude image. POCS-ICE is one of representative method, which could reliably estimate shot phase in both Ms-iEPI and multi-shot spiral DWI [20]. PR-SENSE introduces total variation (TV) as a regularization for the reconstruction of magnitude image in the iterations [21].

In this work, we propose a joint estimation model PAIR with paired phase and magnitude priors to regularize the shot phase and magnitude reconstruction, respectively (Fig. 1). The former prior is derived from the smoothness of the shot phase and enforced with low-rankness in the k-space domain. The latter explores similar edges among multi-b-value and multi-direction DWI with weighted total variation in the image domain. The weighted TV transfers edge information from the high SNR images (b-value=0) to DWI reconstructions, achieving simultaneously noise suppression and image edges preservation.

Extensive simulated and *in vivo* results show that PAIR can remove inter-shot (8 shots) motion artifacts very well even when the partial shot data are corrupted; suppress the noise significantly under the ultra-high b-value (4000 s/mm^2); obtain high-fidelity reconstruction under both uniform and partial Fourier undersampling; achieve nice robustness on multi-vendor multi-center data.

II. Related Works

A. Shot phase constrained low-rankness in PLRHM

The j-th shot DWI image $\mathbf{I}_j$ can be represented as [18]:

$$\mathbf{I}_j = \mathbf{P}_j\mathbf{m} = \mathbf{P}_j^{\phi}\mathbf{P}^{\varphi}\mathbf{m}, \tag{1}$$

where $\mathbf{P}_j^{\phi}$ is the motion-induce phase of j-th shot, $\mathbf{P}^{\varphi}$ is the background phase of DWI images, $\mathbf{P}_j$ is a diagonal matrix, representing the shot phase, and $\mathbf{m}$ is the magnitude image shared by all shot images [18].

In our previous work PLRHM [17], we get:

$$\mathbf{P}_j\mathbf{P}_j^*\mathbf{m} - \mathbf{P}_j\mathbf{P}_j^*\mathbf{m} = \mathbf{0}, \tag{2}$$

where superscript * is the complex conjugate.

Substitute shot image $\mathbf{I}_j = \mathbf{P}_j\mathbf{m}$ and the complex conjugate of the shot image $\mathbf{I}_j^* = \left(\mathbf{P}_j\mathbf{m}\right)^* = \mathbf{P}_j^*\mathbf{m}^* = \mathbf{P}_j^*\mathbf{m}$ into Eq.(2), we get:

$$\mathbf{P}_j\mathbf{I}_j^* = \mathbf{P}_j^*\mathbf{I}_j. \tag{3}$$

Transform the left and right of Eq. (3) into k-space:

$$\tilde{\mathbf{P}}_j \otimes \mathbf{X}_j^* = \tilde{\mathbf{P}}_j^* \otimes \mathbf{X}_j, \tag{4}$$

where $\otimes$ is convolution, $\mathbf{X}_j \in \mathbb{C}^{N*M}$ and $\tilde{\mathbf{P}}_j \in \mathbb{C}^{N*M}$ are the Fourier transform of $\mathbf{I}_j$ and $\mathbf{P}_j$. M and N are the columns and rows of k-space. Rewrite Eq. (4) into a multiplication form:

$$\begin{aligned}&\sum_{(p,q)\in\mathbb{Z}} \tilde{\mathbf{P}}_j(p,q)\mathbf{X}_j^*(-x-p,-y-q)\\ &-\sum_{(p,q)\in\mathbb{Z}} \tilde{\mathbf{P}}_j^*(p,q)\mathbf{X}_j(x-p,y-q) = 0,\end{aligned} \tag{5}$$

where (x, y) is the coordinate of $\mathbf{X}_j$, $x \in [0, N]$ and $y \in [0, M]$. $(p,q) \in \mathbb{Z}$ is the coordinate of $\tilde{\mathbf{P}}_j$ and $\mathbb{Z}$ is the region where $\tilde{\mathbf{P}}_j(p,q)$ is nonzero.

The nonzero value of $\tilde{\mathbf{P}}_j$ in k-space is concentrated in the limited support due to the smoothness of $\mathbf{P}_j$ in the image. Thus, $\mathbb{Z}$ can be approached by a radius R circle region $\mathbb{Z}_R$. With this approximate representation, Eq. (5) holds an annihilation relationship [23]:

$$\begin{aligned}&\sum_{(p,q)\in\mathbb{Z}_R} \mathbf{X}_j^*(-x-p,-y-q)\tilde{\mathbf{P}}_j(p,q)\\ &-\sum_{(p,q)\in\mathbb{Z}_R} \mathbf{X}_j(x-p,y-q)\tilde{\mathbf{P}}_j^*(p,q) \approx 0,\end{aligned} \tag{6}$$

Split the real and imaginary parts of Eq. (6), we get:

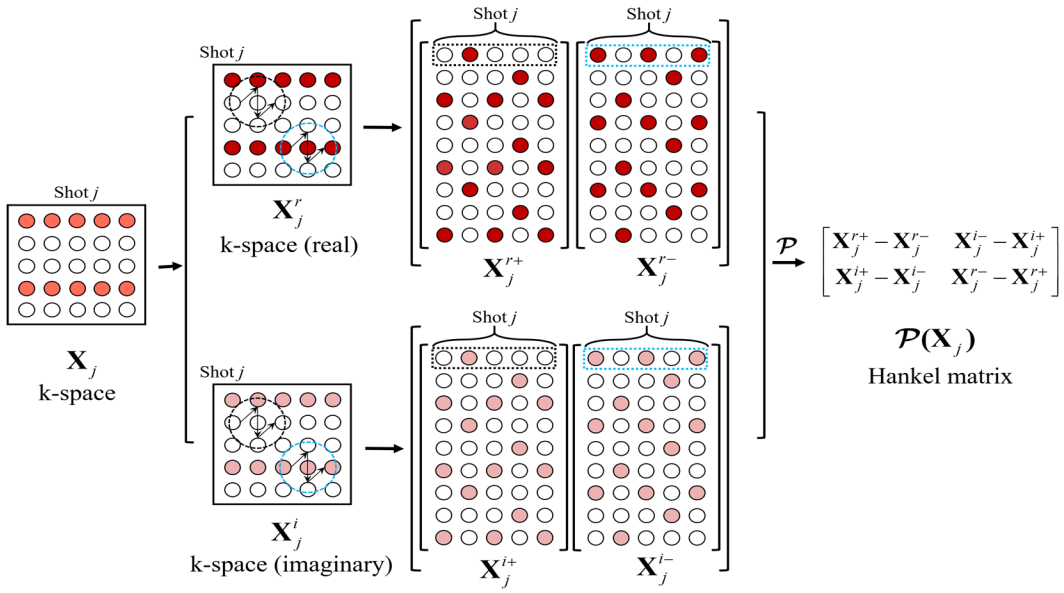

Fig. 2. The flowchart of building Hankel matrix in PLRHM and PAIR. $\mathbf{X}_j$ is the sampled j-shot k-space data. The trajectory of the black sliding window is from top to bottom and left to right, while the blue sliding window is from bottom to top and right to left.

$$\begin{aligned}&\sum_{(p,q)\in\mathbb{Z}_R}\mathbf{X}_j^r(-x-p,-y-q)(\tilde{\mathbf{P}}_j^r(p,q)+\tilde{\mathbf{P}}_j^i(p,q))\\&-\sum_{(p,q)\in\mathbb{Z}_R}\mathbf{X}_j^i(-x-p,-y-q)(\tilde{\mathbf{P}}_j^r(p,q)+\tilde{\mathbf{P}}_j^i(p,q))\\&-\sum_{(p,q)\in\mathbb{Z}_R}\mathbf{X}_j^r(x-p,y-q)(\tilde{\mathbf{P}}_j^r(p,q)-\tilde{\mathbf{P}}_j^i(p,q))\\&-\sum_{(p,q)\in\mathbb{Z}_R}\mathbf{X}_j^i(x-p,y-q)(\tilde{\mathbf{P}}_j^r(p,q)-\tilde{\mathbf{P}}_j^i(p,q))\approx 0,\end{aligned}\tag{7}$$

where the superscript r and i represent real and imaginary part, respectively. The real and imaginary part of Eq. (7) could be split into two equations (Fig. 2), and the matrix multiplication is:

$$\begin{cases}(\mathbf{X}_j^{r+}-\mathbf{X}_j^{r-})\hat{\mathbf{P}}_j^r+(\mathbf{X}_j^{i+}-\mathbf{X}_j^{i-})\hat{\mathbf{P}}_j^i\approx\mathbf{0},\\(\mathbf{X}_j^{i+}+\mathbf{X}_j^{i-})\hat{\mathbf{P}}_j^r+(-\mathbf{X}_j^{r+}-\mathbf{X}_j^{r-})\hat{\mathbf{P}}_j^i\approx\mathbf{0},\end{cases}\tag{8}$$

$$\begin{cases}\mathbf{X}_j^{r+}(e,f)=\mathbf{X}_j^r(x_e-p_f,y_e-q_f),\\\mathbf{X}_j^{r-}(e,f)=\mathbf{X}_j^r(-x_e-p_f,-y_e-q_f),\\\mathbf{X}_j^{i+}(e,f)=\mathbf{X}_j^i(x_e-p_f,y_e-q_f),\\\mathbf{X}_j^{i-}(e,f)=\mathbf{X}_j^i(-x_e-p_f,-y_e-q_f),\\\hat{\mathbf{P}}_j^r(f,1)=\tilde{\mathbf{P}}_j^r(p_f,q_f),\ \ \hat{\mathbf{P}}_j^i(f,1)=\tilde{\mathbf{P}}_j^i(p_f,q_f),\end{cases}\tag{9}$$

where $e\in\left[1,(N-R)*(M-R)\right]$ and $f\in[1,N_R]$, N_R is the number of elements in $\mathbb{Z}_R$. Thus, we get $\mathcal{P}_s$ the operator that converts a single shot k-space data into a Hankel matrix (in the under-braces and Fig. 2). The Eq. (8) implies that this Hankel matrix is rank-deficient [23].

$$\mathcal{P}(\mathbf{X}_j)\begin{bmatrix}\hat{\mathbf{P}}_j^r\\\hat{\mathbf{P}}_j^i\end{bmatrix}=\left\{\begin{bmatrix}\mathbf{X}_j^{r+}-\mathbf{X}_j^{r-} & \mathbf{X}_j^{i-}-\mathbf{X}_j^{i+}\\\mathbf{X}_j^{i+}+\mathbf{X}_j^{i-} & -\mathbf{X}_j^{r-}-\mathbf{X}_j^{r+}\end{bmatrix}\right\}\begin{bmatrix}\hat{\mathbf{P}}_j^r\\\hat{\mathbf{P}}_j^i\end{bmatrix}\approx\mathbf{0}.\tag{10}$$

Moreover, Hankel matrix $\mathcal{P}(\mathbf{X}_j)$ lifted from shots can be concatenated into a larger Hankel matrix $\mathcal{P}(\mathbf{X})$:

$$\mathcal{P}(\mathbf{X})=[\mathcal{P}(\mathbf{X}_1),\ldots\mathcal{P}(\mathbf{X}_J)].\tag{11}$$

PLRHM employs the above phase constrained low-rankness to build an implicit phase reconstruction model [17]:

$$(PLRHM)\ \min_{\mathbf{X}_j}\frac{\lambda}{2}\sum_{h=1}^{H}\left\|\mathbf{Y}_h-\mathcal{U}\mathcal{F}\mathbf{C}_h\mathcal{F}^{-1}\mathbf{X}\right\|_{\mathrm{F}}^2+\sum_{j=1}^{J}\left\|\mathcal{P}\mathbf{X}\right\|_*,\tag{12}$$

where $\mathbf{Y}_h\in\mathbb{C}^{MN*J}$ denotes the sampled and vectorized *h-th* channel multi-shot k-space data, $\mathbf{C}_h\in\mathbb{C}^{MN*MN}$ is the *h-th* channel coil sensitivity maps, λ is the regularization parameter and $\|\cdot\|_*$ is the nuclear norm. $\mathcal{U}$ is an under-sampling operator that fills zeros on non-acquired data points, $\mathcal{F}$ is the Fourier transform operator. $\mathcal{F}^{-1}$ is the inverse Fourier transform operator.

III. Proposed Method

In this work, we propose a joint estimation model of shot phase and magnitude in an alternating fashion for ms-iEPI DWI reconstruction. The paired shot phase (**P**) and magnitude (**m**) priors is incorporated to regularize the updates of shot phase and magnitude, respectively. The whole process is summarized in Fig. 1.

A. Joint estimation model with shot phase prior (PHASE)

Firstly, we improve PLRHM into a joint estimation model PHASE by separating $\mathbf{I}_j$ into shot phase $\mathbf{P}_j$ and magnitude $\mathbf{m}$. The shot phase smoothness prior in PLRHM is similarly used in PHASE to constrain the shot phase update.

$$(PHASE)\ \min_{\mathbf{P},\mathbf{m}}\frac{\lambda}{2}\sum_{h=1}^{H}\sum_{j=1}^{J}\left\|\mathbf{Y}_{hj}-\mathcal{U}\mathcal{F}\mathbf{C}_h\mathbf{P}_j\mathbf{m}\right\|_{\mathrm{F}}^2+\sum_{j=1}^{J}\left\|\mathcal{P}\mathcal{F}\mathbf{P}_j\mathbf{m}\right\|_*,\tag{13}$$

where $\mathbf{Y}_{hj} \in \mathbb{C}^{MN}$ donates the sampled *h-th* channel and *j-th* shot k-space data.

The alternating fashion of PHASE brings two improvements over PLRHM. Firstly, when the shot phases are estimated and combined with sensitivity maps, all shot data can be incorporated together to estimate magnitude. This is a similar multiplexed sensitivity-encoding strategy as MUSE, which may help suppress the noise [18] (Fig. 3). Secondly, the prior that all shot images share the same magnitude are utilized explicitly in PHASE, while shot images in PLRHM have different magnitudes (Fig. 4(a)).

We conducted simulation and *in vivo* reconstructions to explain the advantages of the first and second improvements: nice noise suppression under low SNR scenarios (Fig. 3) and robustness under partially corrupted shot data (Fig. 4).

For simulation comparison, a toy comparison is conducted on a simulated four-shot eight-channel phantom. The whole procedure of simulated multi-shot DWI data is generated as follows: (1) Get a Shepp-Logan phantom image (Fig. 3(a)). (2) Multiply this image with eight-channel coil sensitivity maps (Fig. 3(b)) that are simulated by the Biot-Savart law [21]. (3) Multiply each channel image with the simulated shot phase (Fig. 3(c)), which is generated by steps in [21]. (4) Transform each channel image into its k-space with Fourier transform and then add Gaussian noise to k-space.

PHASE with accurate shot phase (**P** is given by simulated shot phase), and PHASE with estimated shot phase are compared with PLRHM. The implicit phase method, PLRHM, loses the image structure and has a large noise residual (Fig. 3(d)). With the proposed PHASE method, this loss is reduced significantly and the noise is suppressed very well (Fig. 3(d)), if the estimated phase is accurate. Even with the estimated phase, the proposed PHASE (Fig. 3(f)) still outperforms PLRHM in lower loss of image structures and better noise suppression. These observations indicate the good potential of PHASE.

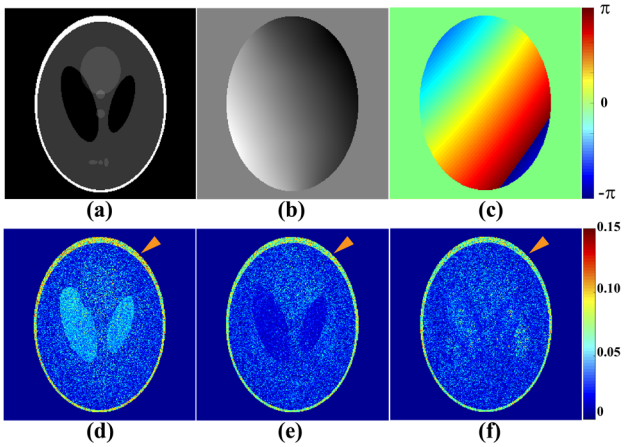

Fig. 3. Reconstructions of the simulated four-shot eight-channel phantom. (a) is the ground-truth magnitude image. (b) is one out of eight simulated coil sensitivity maps. (c) is one out of four simulated shot phases. (d)-(f) are error maps of reconstructed images by PLRHM, PHASE with accurate shot phase, and PHASE with estimated shot phase. Note: Gaussian noise (10 dB) is added to the k-space. The PSNRs of (d)-(f) are 31.03, **32.80**, and 32.50**,** respectively.

The *in vivo* experiment shows that different shot images reconstructed by PLRHM have different magnitudes (Fig. 4(a)). The 8-th shot data is corrupted by common zipper artifacts [25] (yellow arrows in Fig. 4(a)), leading to the same artifacts residual in the SOS magnitude combined from all shot images (Fig. 4(b)). If data rejection [22, 26] is used as a post-processing to exclude the 8-th shot image before SOS, the artifacts in the magnitude image will be suppressed (Fig. 4(c)).

Compared with PLRHM, PHASE shows good robustness to the partially corrupted data (Fig. 4(d)) without post-processing.

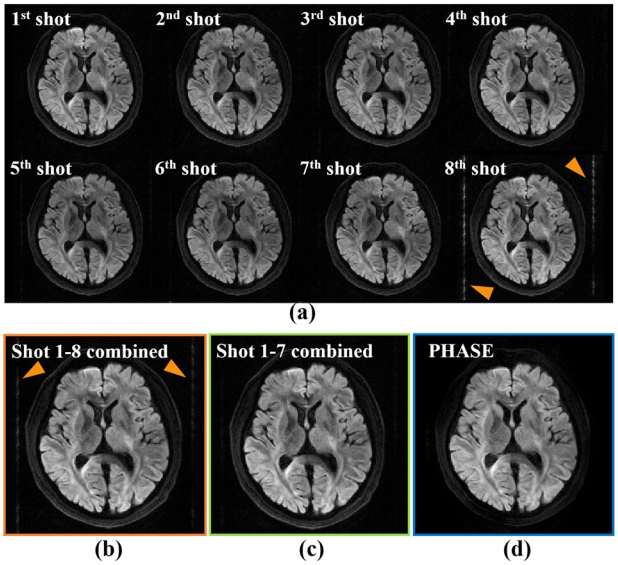

Fig. 4. Partially corrupted shot data reconstructions, the data is 8-shot, 17-channel, in-plane resolution 1.0×1.0mm^2, b-value 1000 s/mm^2. (a) is magnitudes of eight shot images reconstructed by PLRHM. (b) and (c) are the SOS magnitude image from all eight shot and first seven shot images, respectively. (c) is the magnitude reconstructed by PHASE.

B. Joint estimation model with PAIRed phase and magnitude priors (PAIR)

High b-value DWI suffers from low SNR. The signal strength decreases exponentially with the increase of b-value [1]:

$$\boldsymbol{S} = \boldsymbol{S}_0 e^{-b\boldsymbol{D}}, \tag{14}$$

where $\boldsymbol{S}$ and $\boldsymbol{S}_0$ are voxel signal intensity with and without diffusion-weighted, b is the b-value of $\boldsymbol{S}$, and $\mathbf{D}$ is the diffusion coefficient [1]. Non-diffusion image $\mathbf{m}_0$ (b-value=0) has the highest SNR.

Besides above shot phase smoothness prior, the proposed model PHASE enables complementary constraint on magnitude $\mathbf{m}$. Thus, we try to combine magnitude prior in the image domain with PHASE to improve the SNR further.

A widely employed magnitude prior is total variation [21, 27]. It can reduce noise by restraining the sharp jump of the input signal [28, 29]. However, total variation may also bring blur edges to some extent (Figs. 5(a) and (b)).

To avoid edge blur and suppress noise simultaneously, a weighted total variation is added to PHASE to get the paired phase and magnitude image regularizations (PAIR):

$$(\text{PAIR})\ \min_{\mathbf{P},\mathbf{m}} \frac{\lambda}{2}\sum_{h=1}^{H}\sum_{j=1}^{J}\left\|\mathbf{Y}_{hj}-\mathcal{U}\mathcal{F}\mathbf{C}_h\mathbf{P}_j\mathbf{m}\right\|_{\mathrm{F}}^2 + \sum_{j=1}^{J}\left\|\mathcal{P}\mathcal{F}\mathbf{P}_j\mathbf{m}\right\|_* + \beta\left\|\mathbf{m}\right\|_{\mathrm{wTV}}, \tag{15}$$

where β controls image smoothness and the weighted TV term $\|\mathbf{m}\|_{\mathrm{wTV}}$ is defined as:

$$\left\|\mathbf{m}\right\|_{\mathrm{wTV}} = \sum_{x,y}\left(\mathbf{W}_{\perp}^{x,y}\left(\mathbf{m}^{x,y}-\mathbf{m}^{x-1,y}\right)^2 + \mathbf{W}_{=}^{x,y}\left(\mathbf{m}^{x,y}-\mathbf{m}^{x,y-1}\right)^2\right)^{1/2}, \tag{16}$$

where $\mathbf{W}_{\perp}$ and $\mathbf{W}_{=}$ are weights in vertical and horizontal directions, and represent consistent edges among multi-b-value and multi-direction DWI. Its derivations are represented as:

$$\begin{aligned}\frac{\partial\left\|\mathbf{m}\right\|_{\mathrm{wTV}}}{\partial\mathbf{m}} &= \frac{\mathbf{W}_{\perp}^{x,y}\left(\mathbf{m}^{x,y}-\mathbf{m}^{x-1,y}\right)+\mathbf{W}_{=}^{x,y}\left(\mathbf{m}^{x,y}-\mathbf{m}^{x,y-1}\right)}{\left(\mathbf{W}_{\perp}^{x,y}\left(\mathbf{m}^{x,y}-\mathbf{m}^{x-1,y}\right)^2+\mathbf{W}_{=}^{x,y}\left(\mathbf{m}^{x,y}-\mathbf{m}^{x,y-1}\right)^2\right)^{1/2}} \\ &- \frac{\mathbf{W}_{\perp}^{x+1,y}\left(\mathbf{m}^{x+1,y}-\mathbf{m}^{x,y}\right)}{\left(\mathbf{W}_{\perp}^{x+1,y}\left(\mathbf{m}^{x+1,y}-\mathbf{m}^{x,y}\right)^2+\mathbf{W}_{=}^{x+1,y}\left(\mathbf{m}^{x+1,y}-\mathbf{m}^{x+1,y-1}\right)^2\right)^{1/2}} \\ &- \frac{\mathbf{W}_{=}^{x,y+1}\left(\mathbf{m}^{x,y+1}-\mathbf{m}^{x,y}\right)}{\left(\mathbf{W}_{\perp}^{x,y+1}\left(\mathbf{m}^{x,y+1}-\mathbf{m}^{x-1,y+1}\right)^2+\mathbf{W}_{=}^{x,y+1}\left(\mathbf{m}^{x,y+1}-\mathbf{m}^{x,y}\right)^2\right)^{1/2}},\end{aligned} \tag{17}$$

superscripts x and y are the coordinates.

In the proposed method, the prior weights $\mathbf{W}_{\perp}$ and $\mathbf{W}_{=}$ are estimated from the image $\mathbf{m}_0$ (b-value=0) according to:

$$\begin{cases}\mathbf{W}_{\perp}^{x,y} = \exp\left[-\left[\mathbf{m}_0^{x,y}-\mathbf{m}_0^{x-1,y}\right]^2/\delta\right] \\ \mathbf{W}_{=}^{x,y} = \exp\left[-\left[\mathbf{m}_0^{x,y}-\mathbf{m}_0^{x,y-1}\right]^2/\delta\right]\end{cases}, \tag{18}$$

where δ is a small denominator to enlarge the difference between neighbor pixels.

Specifically, for a smooth region, the value of $\mathbf{m}_0(x,y)-\mathbf{m}_0(x-1,y)$ (or $\mathbf{m}_0(x,y)-\mathbf{m}_0(x,y-1)$) is close to 0, leading to $\mathbf{W}_{\perp}(x,y)$ (or $\mathbf{W}_{=}(x,y)$) approach to 1. At image edges, the value of $\mathbf{m}_0(x,y)-\mathbf{m}_0(x-1,y)$ (or $\mathbf{m}_0(x,y)-\mathbf{m}_0(x,y-1)$) is relatively, leading to $\mathbf{W}_{\perp}(x,y)$ (or $\mathbf{W}_{=}(x,y)$) be larger than 1. Thus, the exponential function in Eq. (18) adjusts all weights to the range (0, 1], and makes sure that $\mathbf{W}_{\perp}$ and $\mathbf{W}_{=}$ are large in smooth regions (blue arrows in Fig. 11) but small on edges (white arrows in Fig. 11). Then, through minimizing the objective function in Eq. (15), the target image will be penalized heavily at smooth regions and slightly or even not be penalized at edges. Therefore, the weighted TV can simultaneously suppress noise and avoid edge blurring.

To show the benefits of the edge preserving prior, the methods including PHASE, PAIR with total variation, and PAIR with weighted total variation, are compared in Fig. 5.

PAIR with total variation could greatly suppress the noise but results in loss of edge intensities (white arrow in Fig. 5(b)). PAIR with weighted total variation shows good tolerance to noise and preserves edges much better (Fig.5 (c)). In the following sections, PAIR with weighted total variation is abbreviated as PAIR for short.

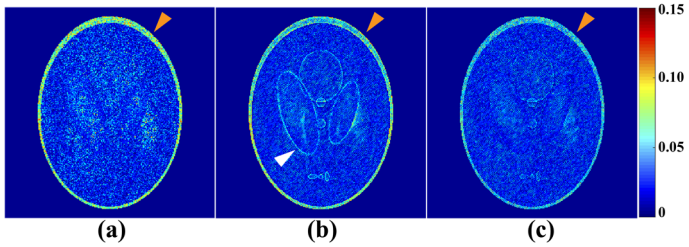

Fig. 5. Reconstructions of the simulated four-shot eight-channel phantom. (a)-(c) are the error maps of PHASE, PAIR with total variation, and PAIR with weighted total variation, respectively. The yellow arrows show different noise residual levels and the white arrow shows blurred edges. Note: Simulated phantom is the same as Fig. 4. PSNRs of (a)-(c) are 32.50, 33.12, and **34.23,** respectively.

C. Numerical algorithm

We adopt the Projections Onto Convex Sets (POCS) algorithm to solve the PAIR in Eq. (15) [20, 30-32].

The iterative reconstruction is consisting of data consistency, phase update with low-rankness constraint, and magnitude update with weighted total variation (Fig. 1). In the iterative process, the phases become increasingly smooth (upper row in Fig. 1) and artifacts in magnitude image gradually decrease (lower row in Fig. 1).

The *k-th* ($k=1,2,\ldots K$) iteration is shown as follows:

1) Data consistency

$$\mathbf{G}_{hj}^{k} = \mathbf{C}_h\mathbf{P}_j^{k}\mathbf{m}^{k} + \lambda\mathcal{F}^*\mathcal{U}^*\left(\mathbf{Y}_{hj}-\mathcal{U}\mathcal{F}\mathbf{C}_h\mathbf{P}_j^{k}\mathbf{m}^{k}\right), \tag{19}$$

$$\mathbf{I}_j^{k} = \sum_{h=1}^{H}\mathbf{C}_i^*\mathbf{G}_{hj}^{k},\ j=1,2,\ldots,J. \tag{20}$$

2) Phase update with low-rankness constraint

$$\mathbf{I}_j^{k+1} = \mathcal{F}^*\mathcal{P}^*\left(\mathrm{SVT}_{\varepsilon}\left(\mathcal{P}\mathcal{F}\left(\mathbf{I}_j^{k}\right),\sigma\right)\right),\ j=1,2,\ldots,J, \tag{21}$$

$$\mathbf{P}_j^{k+1} = \mathbf{I}_j^{k+1}\Big/\left|\mathbf{I}_j^{k+1}\right|,\ j=1,2,\ldots,J, \tag{22}$$

where $\mathrm{SVT}_{\varepsilon}(\mathbf{Z},\sigma)$ is the singular value thresholding operator on a matrix $\mathbf{Z}$ [33, 34]. The first ε singular values are saved and others minus a proper threshold σ.

3) Magnitude update with weighted total variation

Firstly, the averaged magnitude $\mathbf{m}_{avg}^{k}$ of all shot images are obtained by:

$$\mathbf{m}_{avg}^{k} = \sum_{j=1}^{J}\mathbf{P}_j^{k*}\odot\mathbf{I}_j^{k}. \tag{23}$$

Then, weighted TV is performed on the averaged magnitude:

$$\mathbf{m}_{wTV}^{k} = \mathbf{m}_{avg}^{k} - \beta\left(\frac{\partial\left\|\mathbf{m}^{k}\right\|_{\mathrm{wTV}}}{\partial\mathbf{m}^{k}}\right), \tag{24}$$

$$\mathbf{m}^{k+1} = \mathbf{m}^{k} + \eta\left(\mathbf{m}_{wTV}^{k}-\mathbf{m}^{k}\right), \tag{25}$$

where $\eta\in[1,2)$ controls convergence speed.

IV. Experiments

A. In vivo datasets

Comprehensive experiments are conducted to evaluate the performance of PAIR. Four datasets acquired on three vendors

from four centers are employed for *in vivo* experiments. Their imaging parameters are shown in Table I. All the *in vivo* data collected by ourselves in this study are approved by the institutional review board.

For all datasets, odd-even EPI shifts have been corrected carefully. Coil sensitivity maps are calculated by ESPIRIT using $\mathbf{m_0}$ [35]. The directionally encoded color maps are produced using a Matlab toolbox[1].

B. Experiments settings

For comparative study, navigator-based (IRIS [11]) and navigator-free (MUSE [18], POCS-ICE [20], MUSSELS-IRLS-CS [16], PLRHM [17]) methods are adopted. MUSE is a widely accepted two-step explicit method. POCS-ICE is a joint phase and magnitude reconstruction method. MUSSELS-IRLS-CS and PLRHM are implicit phase reconstruction methods which introduce the low-rankness priors into reconstruction. All the reconstructed multi-shot images by implicit phase methods are displayed after combining by the SOS. MUSE, POCS-ICE and PLRHM are implemented by ourselves, and MUSSELS-IRLS-CS is provided by Dr. Mathews Jacob online[2]. All methods are implemented in MATLAB and the parameters are optimized for best performance in terms of least artifacts.

We take average angular error (AAE) and peak signal-to-noise (PSNR) [15] as objective criteria:

$$\text{AAE (degree)} := \frac{1}{L}\sum_{n=1}^{N}\cos^{-1}\left(\left\langle \mathbf{v}_l \cdot \hat{\mathbf{v}}_l \right\rangle\right) * 180/\pi \,, \tag{26}$$

$$\text{PSNR (dB)} := 10\cdot\log_{10}\left(\frac{NM}{\left\|\hat{\mathbf{m}}-\mathbf{m}\right\|_2^2}\right), \tag{27}$$

where $\|\cdot\|_2$ is the l_2 norm, $\mathbf{m}$ and $\hat{\mathbf{m}}$ are vectorized reference and reconstructed images, respectively. $\mathbf{v}_l$ and $\hat{\mathbf{v}}_l$ represent the primary diffusion direction vector of reference and reconstructed maps. L is the number of vectors. The higher PSNR and lower AAE indicate a lower noise level and smaller angular error, respectively.

C. High-resolution DWI

Reconstructed results of navigator-based method IRIS are employed as references (Fig. 6(a)), because the shot phase is accurately estimated by the navigator and the reconstructed

TABLE Ⅰ IMAGING PARAMETERS OF THREE DATASETS.

Dataset	Vendor/Center	Channel	Shot	Matrix Size	Resolution (mm^3)	B-values (s/mm^2)	Signal average	Diffusion directions
I	Philips 3.0T /Beijing, China.	8	8	230×232	1.0×1.0×4	0, 800	1	15
II	UI 3.0T /Shanghai, China	17	4/8	160×160, 230×224	1.4×1.4×5 , 1.0×1.0×5	0, 1000, 2000, 3000, 4000	1	3
III	Philips 3.0T /Xiamen, China	32	4	180×180	1.2×1.2×5	0, 1000	2	12
VI	XinGaoYi 1.5T /Yuyao, China	16	4	140×192	/	0, 1000	2	3

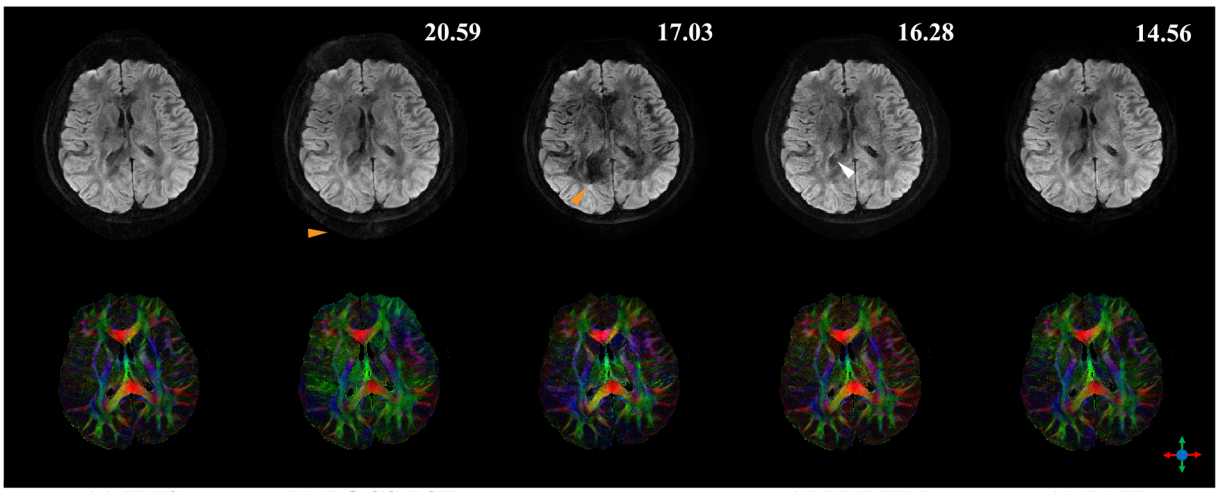

Fig. 6. Reconstructions of high-resolution DWI images and color fractional anisotropy images estimated from 15 diffusion directions in Dataset I. The top row are the first direction DWI and the bottom row are directionally encoded color maps. Artifacts and blurred edge have been remarked with yellow and white arrows, respectively. AAEs are in the upper right corner.

[1] https://www.mathworks.com/matlabcentral/fileexchange/34008-dti-fiber-tractography-streamline-tracking-technique
[2] https://github.com/sajanglingala/data_adaptive_recon_MRI

images have no obvious artifact. Some obvious artifacts can be observed in the results of POCS-ICE and MUSSELS-IRLS-CS (yellow arrows in Figs. 6(b) and (c)). PLRHM and PAIR have a good tolerance to artifacts. PLRHM shows a relatively low SNR. Some edges have been blurred, such as the posterior horn of lateral ventricles (Fig. 6(d)). The result of the proposed PAIR achieves a lower noise level and more clear edges (Fig. 6(e)).

Directionally encoded color maps are estimated with fifteen diffusion directions. They are calculated by fractional anisotropy images times the primary diffusion direction. Some color mismatches with reference maps could be observed in Figs. 6(a)-(d). The result of PAIR is closest to the reference maps visually and achieves the lowest angular error AAE.

Thus, PAIR outperforms other state-of-the-art navigator-free methods on high-resolution DWI reconstruction.

D. Ultra-high b-values DWI

The ultra-high b-values DWI data (3000 and 4000 s/mm^2) have a significantly low SNR, which poses a severe challenge for reconstruction. The navigator-based IRIS can hardly reconstruct the image (Fig. 7(a)), which may be caused by the low SNR and geometric mismatch between the navigator and image echo. POCS-ICE introduces obvious ghosting artifacts (Fig. 7(b)). Both MUSSELS-IRLS-CS and PLRHM better remove artifacts but suffer from relatively low SNR (Figs. 7(c) and (d)). The proposed PAIR outperforms other methods on much better tolerance to artifacts and noise (Fig. 7(e)).

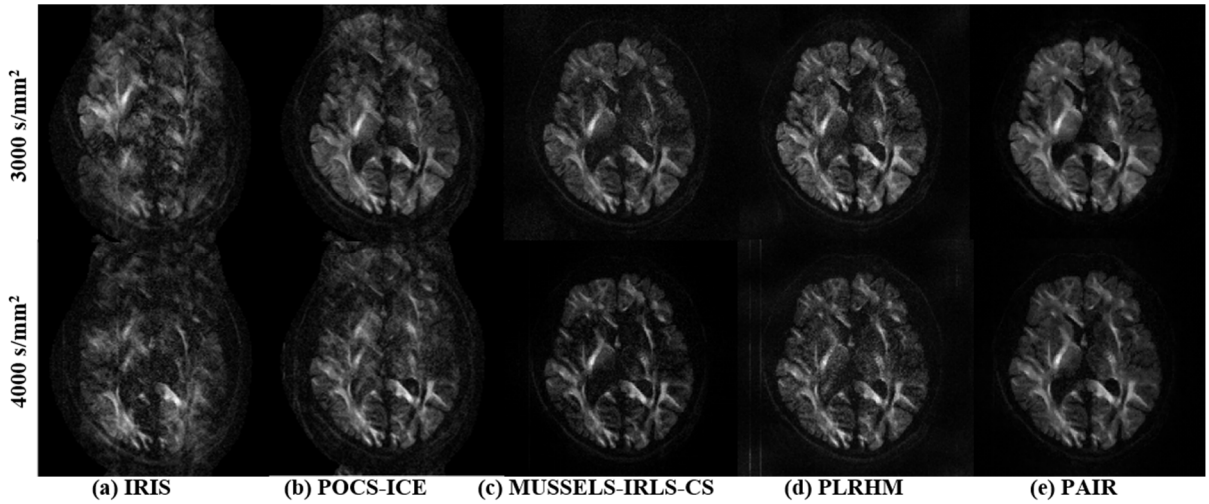

Fig. 7. Reconstructions of high b-values eight-shot data in Dataset II.

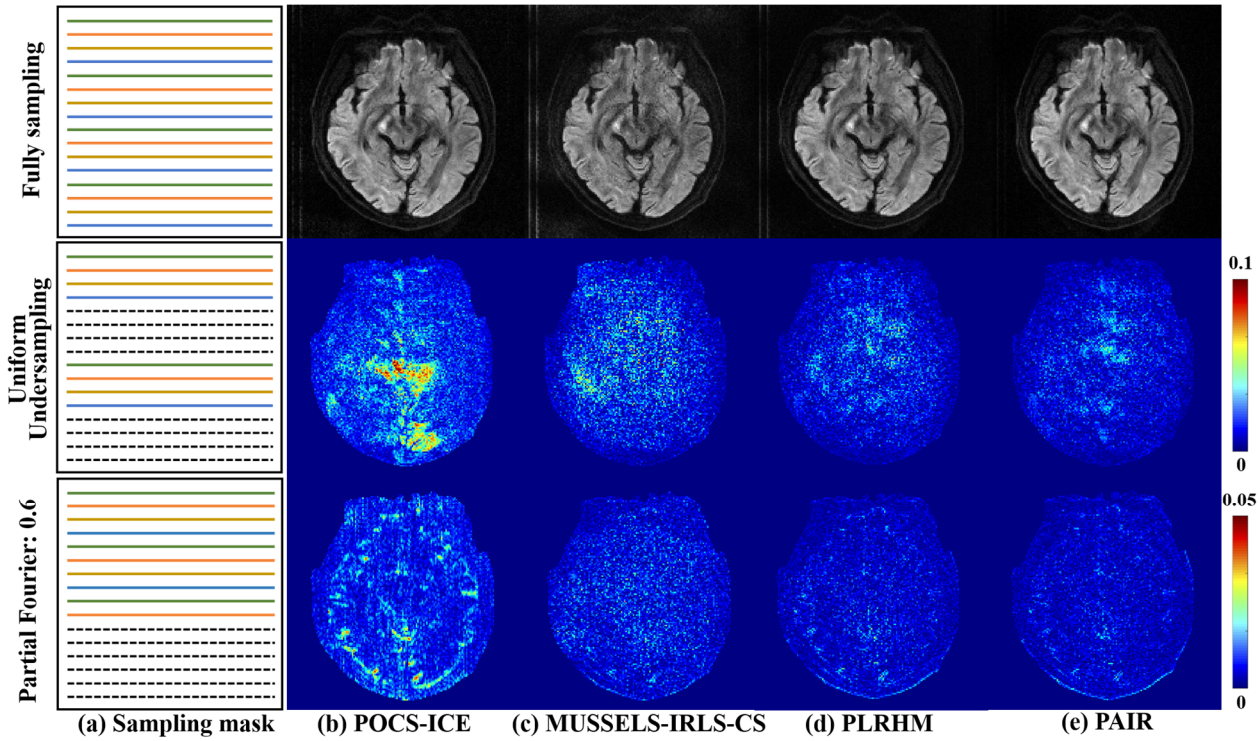

Fig. 8. Reconstructions of fully sampling and undersampling four-shot data in Dataset II. Note: Solid and dotted lines represent sampled shot and unsampled shot data, respectively. Different colors represent different shots.

These results show that the PAIR is applicable for ultra-high b-values DWI reconstruction and does not need navigator signals.

E. Accelerated DWI

For accelerated DWI with undersampling, the four-shot data in Dataset II is reconstructed with retrospectively uniform and partial Fourier undersampling. The sampling rate of them are 0.5 and 0.6, respectively. For evaluation, the fully sampled four-shot data are reconstructed as references (first row in Fig. 8).

On the fully sampled data, All the methods show comparable performances (first row in Fig. 8). Two explicit phase methods POCS-ICE and PAIR have relatively better resistance to zipper artifacts than MUSSELS-IRLS-CS and PLRHM.

On the undersampled data, error maps corresponding to the fully sampling references are calculated. Compared with other methods, PAIR provides the highest fidelity results on both uniform and partial Fourier undersampling reconstructions (Fig. 8).

F. Comparison study with explicit phase method MUSE

In this section, we compare the PAIR with a classical two-step explicit method MUSE to illustrate the advantages of joint estimation over the simple explicit method.

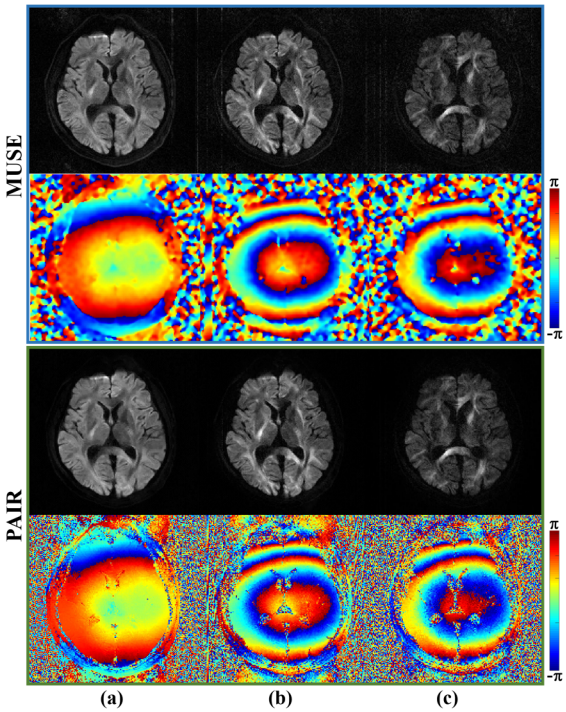

Fig. 9. Reconstructed magnitudes and shot phases of multi b-values DWI data by MUSE and PAIR. The data are 4-shot, 17-channel, in-plane resolution 1.5×1.5 mm^2 from Dataset II. The b-value of (a)-(c) are 1000, 2000, and 3000 s/mm^2, respectively.

Fig. 9 shows the performance of PAIR and MUSE on 4-shot DWI reconstruction. Both MUSE and PAIR could remove motion artifacts well in magnitude images. However, noise residue on magnitudes of MUSE are relatively large, and some zipper artifacts can also be observed. PAIR has better noise suppression, especially in high b-value reconstructions (3000 s/mm^2).

The increased b-values lead to an increase in phase winding in Fig. 9. For MUSE, the shot phases are estimated from each shot by SENSE reconstruction, and then will be fixed as known variables to estimate magnitude. However, in PAIR, the shot phase is updated in iterations. The shot phases reconstructed by PAIR have more structure details, especially in cerebrospinal fluid region (Fig. 9). Even though the true shot phase can never be known, the shot phases estimation by PAIR may be more precise because it can provide higher quality magnitudes.

G. Comparison study on the weighted TV

In Fig. 10, the high resolution (1.0×1.0 mm^2) and high b-values (3000 s/mm^2) reconstructions show that, compared with PHASE, weighted TV provides PAIR better noise suppression while preserving edges.

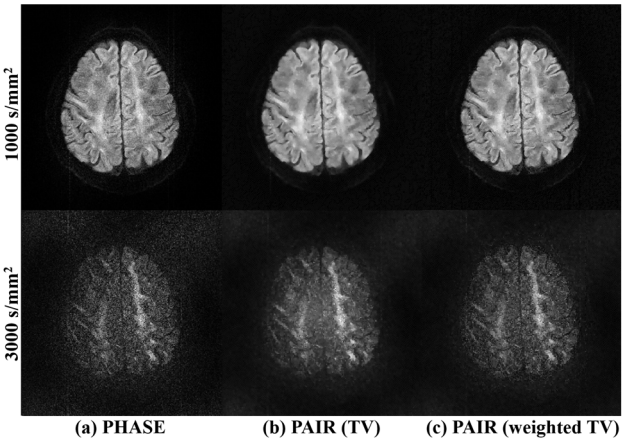

Fig. 10. Reconstructions by PHASE, PAIR with TV, and PAIR with weighted TV. The data from Dataset II are 4-shot, 17-channel, 1.0×1.0 mm^2, 1000 and 3000 s/mm^2. Note: $\delta = 0.02$, and weighted TV and TV have the same $\beta = 0.3$.

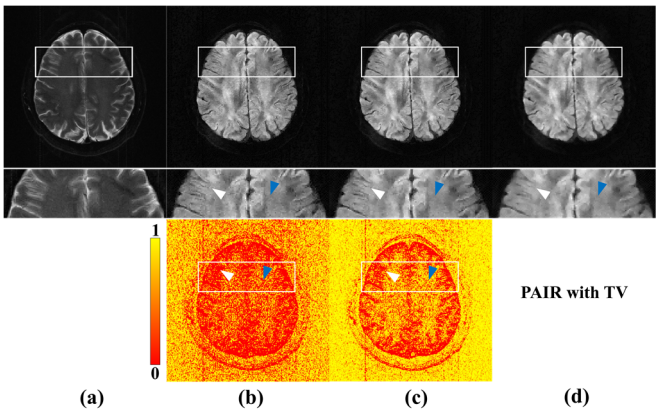

Fig. 11. Reconstructions with different TV. The data is 4-shot, 17-channel, in-plane resolution 1.0×1.0 mm^2, b-value 1000 s/mm^2 DWI in Dataset II. (a) is the reference image $\mathbf{m}_0$ (b-value=0). (b)-(d) are results of PAIR with wTV ($\delta = 0.01$), PAIR with wTV ($\delta = 0.02$), and PAIR with TV. The up, middle and down row of (c)-(e) are reconstruction results, corresponding zoom in regions, and the weights $\mathbf{W}_{=}$ calculated from $\mathbf{m}_0$. Note: weighted TV and TV have the same $\beta = 0.3$.

To further illustrate how weighted TV works, we draw the weights extracted from $\mathbf{m}_0$ under the different δ (Fig. 11). The

weights are large in the smooth regions, while small in the image edges. Compared with PAIR with TV (equivalent to the case where the weights are all 1), PAIR with weighted TV could similarly suppress noise in the smooth region (white arrows in Fig. 11), and preserve texture details (blue arrows in Fig. 11).

V. Discussions

A. Discussion on Parameter Settings

The effect of parameter settings in the singular value thresholding operator $\mathrm{SVT}_{\varepsilon}(\mathbf{Z},\sigma)$ is discussed in the simulation and *in vivo* experiments here. The operator is performed on the structured low-rank matrix $\mathbf{Z}$ to constrain phase smoothness. The first ε singular values are saved and others minus a proper threshold σ.

In the simulation study, the radius of limited support R is 2, and the size of $\mathbf{Z}$ is 104×98550. PAIR achieves nice PSNR when ε is in the range of 20-30, under a proper σ (0.3-0.9) (Fig. 12(a)). When σ is too large (≥1.2), only singular values larger than σ are saved, resulting in invariant PSNR (second half of the purple and green curve in Fig. 12(a)).

In *in vivo* study, the radius of limited support R is 2, and the size of $\mathbf{Z}$ is 104×48050 and σ is 0.6. In a wide range of ε (10-30), PAIR has comparable results (Fig. 12(b)). When ε becomes larger (40-60), some artifacts will remain in the images (yellow arrows in Fig. 12(b)).

The above experiments indicate PAIR is insensitive to parameters and has robust performance.

Other typical parameters are $\lambda=1$, $\eta=1.5$, $\beta\in[10^{-4},5\times10^{-1}]$, The initialization of shot phase $\mathbf{P}$ and magnitude $\mathbf{m}$ are $\mathbf{1}$ and $\mathbf{0}$, respectively. the iteration stop condition is $\left\|\mathbf{m}^{k+1}-\mathbf{m}^{k}\right\|_F^2 \Big/ \left\|\mathbf{m}^{k}\right\|_F^2 \geq 10^{-5}$, and the max iteration is 1000.

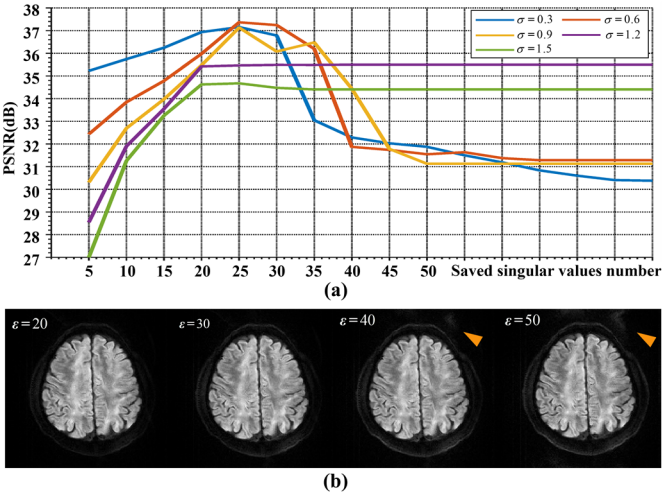

Fig. 12. PAIR Reconstructions on simulation and *in vivo* data with different ε and σ. (a) The simulation data is 4-shot, 8-channel. (b) The *in vivo* data from Dataset II is 4-shot, 17-channel, 1.5×1.5 mm^2, 1000 s/mm^2, and σ is 0.6.

B. Discussion on reconstruction time of PAIR

The reconstruction time of PAIR is tested on the three kinds of DWI data (Tab. II). The iteration stop condition is $\left\|\mathbf{m}^{k+1}-\mathbf{m}^{k}\right\|_F^2 \Big/ \left\|\mathbf{m}^{k}\right\|_F^2 \geq 10^{-5}$, and the max iterations is 1000. In all tests, PAIR could reach convergence and complete reconstruction quickly (Tab. II).

All the computation procedures are executed by MATLAB, running on a CentOS 7 computation server with twenty Intel Core i9-9900X CPUs of 3.5 GHz and 125 GB RAM. No parallel computing is employed.

TABLE II. RECONSTRUCTION TIME OF PAIR

Dataset	Matrix size (RO×PE×Channel×Shot)	Iterations when stop	Time (s)
II	160×160×17×4	22	12.4
II	230×224×17×4	27	26.1
III	180×180×32×4	45	34.3

C. Discussion on multi-vendor multi-center reconstruction

Multi-center data harmonization is an important issue for healthcare studies [36, 37]. We test the performance of PAIR on diverse DWI data acquired by scanners from 3 vendors in 4 centers (Fig. 13).

PAIR shows robust performance on the above multi-vendor multi-center data, and the motion artifacts could be removed well (Fig. 13).

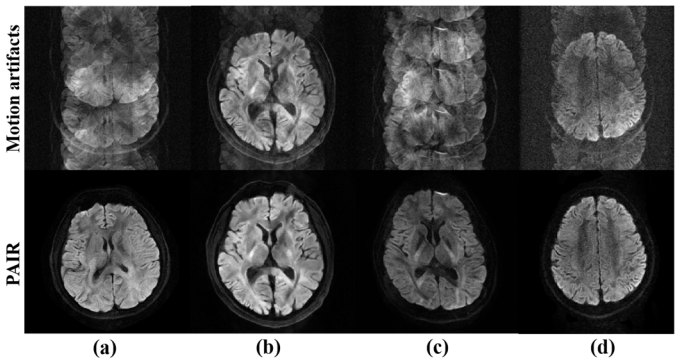

Fig. 13. PAIR reconstructions on the multi-center multi-vendor in vivo data. (a) is from Dataset I: Philips 3.0T scanner in Beijing, China. 8-shot, 8-channel, b-value 800 s/mm^2, in-plane resolution 1.0×1.0 mm^2. (b) is from Dataset II: United Imaging 3.0T scanner in Shanghai, China. 4-shot, 17-channel, b-value 1000 s/mm^2, in-plane resolution 1.5×1.5 mm^2. (c) is from Dataset III: Philips 3.0T scanner in Xiamen, China. 4-shot, 32-channel, b-value 1000 s/mm^2, in-plane resolution 1.2×1.2 mm^2. (d) is from Dataset VI: XinGaoYi 1.5T scanner in Yuyao, China. 4-shot, 8-channel, b-value 1000 s/mm^2.

VI. Conclusion and Outlook

In this work, we aim at solving the multi-shot DWI reconstructions under inter-shot motions and ultra-high b-values. A joint phase and magnitude estimation model with paired low-rank and weighted TV priors is proposed to regularize the reconstruction. The joint estimation model ensures that all shots share the same magnitude strictly. The weighted TV in the image domain explores similar edges among multi-b-value and multi-direction DWI. Comprehensive experiments show that PAIR has faithful shot phase estimation and can remove inter-shot (8 shots) motion artifacts very well even when the partial shot data are corrupted. Compared with

state-of-the-art methods, it shows much better and more robust performance on some low SNR scenarios, such as the undersampling (uniform and partial Fourier) and ultra-high b-values DWI (4000 s/mm^2). Moreover, reconstructions on multi-vendor multi-center DWI data indicate its nice robustness.

The good performance and nice robustness of PAIR on high-resolution, ultra-high b-value and accelerated DWI reconstructions show great potential for advanced clinical DWI applications and brain function research.

In the future, we will develop PAIR to solve abdomen DWI reconstructions, such as high-resolution prostate and liver DWI. These reconstructions suffer from lower SNR and non-smooth shot phase, which may be challenging for PAIR and need great improvements.

In addition, to make it easier to use PAIR, we have implemented and deployed PAIR on the open-access cloud platform, CloudBrain-ReconAI [38-41]. (please visit https://csrc.xmu.edu.cn/CloudBrain.html). On the CloudBrain-ReconAI, we also provide physics-informed deep DWI reconstruction methods [38, 41] as comparison algorithms to PAIR reconstructions.

ACKNOWLEDGEMENTS

The authors thank Yiman Huang, Dicheng Chen for the discussions on the MRI reconstruction; Dr. Hua Guo, Yi Xiao for their assistances in data acquisition and image analysis; Yu Hu for creating video tutorials on CloudBrain-ReconAI usage; Dr. Mathews Jacob for sharing the IRLS-MUSSELS-CS code online; The authors also thank the editors and reviewers for the valuable suggestions.

REFERENCES

[1] D. K. Jones, "Diffusion MRI". Oxford University Press, 2010.
[2] M. G. Lansberg, G. W. Albers, C. Beaulieu, and M. P. Marks, "Comparison of diffusion-weighted MRI and CT in acute stroke," *Neurology*, vol. 54, no. 8, pp. 1557-1561, 2000.
[3] M. Cihangiroglu *et al*., "The utility of high b-value DWI in evaluation of ischemic stroke at 3 T," *Eur. J. Radiol.*, vol. 78, no. 1, pp. 75-81, 2011.
[4] C. K. Kim, B. K. Park, and B. Kim, "High-b-value diffusion-weighted imaging at 3 T to detect prostate cancer: Comparisons between b values of 1,000 and 2,000 s/mm^2," *Am. J. Roentgenol.*, vol. 194, no. 1, pp. 33-37, 2010.
[5] Y. Ohgiya *et al*., "Diagnostic accuracy of ultra-high-b-value 3.0-T diffusion-weighted MR imaging for detection of prostate cancer," *Clin. Imaging*, vol. 36, no. 5, pp. 526-531, 2012.
[6] G. C. Baxter, A. J. Patterson, R. Woitek, I. Allajbeu, M. J. Graves, and F. Gilbert, "Improving the image quality of DWI in breast cancer: comparison of multi-shot DWI using multiplexed sensitivity encoding to conventional single-shot echo-planar imaging DWI," *Brit. J. Radiol*, vol. 94, no. 1119, 20200427, 2021.
[7] P. Mukherjee, J. Berman, S. Chung, C. Hess, and R. Henry, "Diffusion tensor MR imaging and fiber tractography: Theoretic underpinnings," *Am. J. Neuroradiol.*, vol. 29, no. 4, pp. 632-641, 2008.
[8] M. M. Thurnher and M. Law, "Diffusion-weighted imaging, diffusion-tensor imaging, and fiber tractography of the spinal cord," *Magn. Reson. Imaging Clin. N. Am.*, vol. 17, no. 2, pp. 225-244, 2009.
[9] H. An, X. Ma, Z. Pan, H. Guo, and E. Y. P. Lee, "Qualitative and quantitative comparison of image quality between single-shot echo-planar and interleaved multi-shot echo-planar diffusion-weighted imaging in female pelvis," *Eur. Radiol.*, vol. 30, no. 4, pp. 1876-1884, 2020.
[10] A. W. Anderson and J. C. Gore, "Analysis and correction of motion artifacts in diffusion weighted imaging," *Magn. Reson. Med.*, vol. 32, no. 3, pp. 379-87, 1994.
[11] H.-K. Jeong, J. C. Gore, and A. W. Anderson, "High-resolution human diffusion tensor imaging using 2-D navigated multishot SENSE EPI at 7 T," *Magn. Reson. Med*., vol. 69, no. 3, pp. 793-802, 2013.
[12] X. Ma, Z. Zhang, E. Dai, and H. Guo, "Improved multi-shot diffusion imaging using GRAPPA with a compact kernel," *Neuroimage*, vol. 138, pp. 88-99, 2016.
[13] L. Guo *et al*., "eIRIS: Eigen-analysis approach for improved spine multi-shot diffusion MRI," *Magn. Reson. Imaging*, vol. 50, pp. 134-140, 2018.
[14] S. Skare, R. D. Newbould, D. B. Clayton, G. W. Albers, S. Nagle, and R. Bammer, "Clinical multishot DW-EPI through parallel imaging with considerations of susceptibility, motion, and noise," *Magn. Reson. Med*., vol. 57, no. 5, pp. 881-890, 2010.
[15] M. Mani, M. Jacob, D. Kelley, and V. Magnotta, "Multi-shot sensitivity-encoded diffusion data recovery using structured low-rank matrix completion (MUSSELS)," *Magn. Reson. Med.*, vol. 78, no. 2, pp. 494-507, 2017.
[16] M. Mani, H. K. Aggarwal, V. Magnotta, and M. Jacob, "Improved MUSSELS reconstruction for high-resolution multi-shot diffusion weighted imaging," *Magn. Reson. Med*., vol. 83, no. 6, pp. 2253-2263, 2020.
[17] Y. Huang *et al*., "Phase-constrained reconstruction of high-resolution multi-shot diffusion weighted image," *J. Magn. Reson.* vol. 312, 106690, 2020.
[18] N.-k. Chen, A. Guidon, H.-C. Chang, and A. W. Song, "A robust multi-shot scan strategy for high-resolution diffusion weighted MRI enabled by multiplexed sensitivity-encoding (MUSE)," *Neuroimage*, vol. 72, pp. 41-47, 2013.
[19] M. L. Chu, H. C. Chang, H. W. Chung, T. K. Truong, M. R. Bashir, and N. K. Chen, "POCS-based reconstruction of multiplexed sensitivity encoded MRI (POCSMUSE): A general algorithm for reducing motion-related artifacts," *Magn. Reson. Med.*, vol. 74, no. 5, pp. 1336-1348, 2015.
[20] H. Guo, X. Ma, Z. Zhang, B. Zhang, C. Yuan, and F. Huang, "POCS-enhanced inherent correction of motion-induced phase errors (POCS-ICE) for high-resolution multishot diffusion MRI," *Magn. Reson. Med*., vol. 75, no. 1, pp. 169-180, 2016.
[21] Z. Hu, X. Ma, T.-K. Truong, A. W. Song, and H. Guo, "Phase-updated regularized SENSE for navigator-free multishot diffusion imaging," *Magn. Reson. Med*., vol. 78, no. 1, pp. 172-181, 2017.
[22] Z. Zhang, F. Huang, X. Ma, S. Xie, and H. Guo, "Self-feeding MUSE: A robust method for high resolution diffusion imaging using interleaved EPI," *NeuroImage*, vol. 105, pp. 552-560, 2015.
[23] J. P. Haldar, "Low-rank modeling of local k-space neighborhoods (LORAKS) for constrained MRI," *IEEE Trans. Med. Imaging*, vol. 33, no. 3, pp. 668-681, 2013.
[24] K. H. Jin, D. Lee, and J. C. Ye, "A general framework for compressed sensing and parallel MRI using annihilating filter based low-rank Hankel matrix," *IEEE Trans. Comput. Imaging*, vol. 2, no. 4, pp. 480-495, 2016.
[25] K. H. Jin, J. Y. Um, D. Lee, J. Lee, S. H. Park, and J. C. Ye, "MRI artifact correction using sparse + low-rank decomposition of annihilating filter-based Hankel matrix," *Magn. Reson. Med.,* vol. 78, no. 1, pp. 327-340, 2017.
[26] L. C. Chang, D. K. Jones, and C. Pierpaoli, "RESTORE: Robust estimation of tensors by outlier rejection," *Magn. Reson. Med.*, vol. 53, no. 5, pp. 1088-1095, 2005.
[27] B. Bilgic *et al*., "Highly accelerated multishot echo planar imaging through synergistic machine learning and joint reconstruction," *Magn. Reson. Med*., vol. 82, no. 4, pp. 1343-1358, 2019.

[28] H. Guo, P. Liu, M. Wang, and C. Li, "TV-RSPIRiT: Total variation regularized based robust self-consistent parallel imaging reconstruction," in *International Conference on Medical Imaging Physics and Engineering*, pp. 1-4, 2019.
[29] Y. Zhang *et al*., "Contrast-medium anisotropy-aware tensor total variation model for robust cerebral perfusion CT reconstruction with low-dose scans," *IEEE Trans. Comput. Imaging*, vol. 6, pp. 1375-1388, 2020.
[30] A. A. Samsonov, E. G. Kholmovski, D. L. Parker, and C. R. Johnson, "POCSENSE: POCS-based reconstruction for sensitivity encoded magnetic resonance imaging," *Magn. Reson. Med*., vol. 52, no. 6, pp. 1397-1406, 2004.
[31] N. T. Thao and M. Vetterli, "Set theoretic compression with an application to image coding," *IEEE Trans. Image Process.*, vol. 7, no. 7, pp. 1051-1056, 1998.
[32] H. Xue, L. Zhang, Z. Cheng, Y. Xing, and Y. Xiao, "An improved TV minimization algorithm for incomplete data problem in computer tomography," in *IEEE Nuclear Science Symposuim & Medical Imaging Conference*, 2010, pp. 2621-2624.
[33] J. F. Cai, E. J. Candès, and Z. Shen, "A singular value thresholding algorithm for matrix completion," *SIAM J. Optim.*, vol. 20, no. 4, pp. 1956-1982, 2010.
[34] X. Qu, M. Mayzel, J. F. Cai, Z. Chen, and V. Orekhov, "Accelerated NMR spectroscopy with low-rank reconstruction," *Angew. Chem.-Int. Edit.*, vol. 54, no. 3, pp. 852-854, 2015.
[35] M. Uecker et al., "ESPIRiT-an eigenvalue approach to autocalibrating parallel MRI: Where SENSE meets GRAPPA," Magn. Reson. Med., vol. 71, no. 3, pp. 990-1001, 2014.
[36] Y. Nan *et al*., "Data harmonisation for information fusion in digital healthcare: A state-of-the-art systematic review, meta-analysis and future research directions," *Inform. Fusion*, vol. 82, pp. 99-122, 2022.
[37] Y. Chen *et al.*, "AI-based reconstruction for fast MRI-a systematic review and meta-analysis," *Proc. IEEE*, vol. 110, no. 2, pp. 224-245, 2022.
[38] Q. Yang, Z. Wang, K. Guo, C. Cai, and X. Qu, "Physics-driven synthetic data learning for biomedical magnetic resonance: The imaging physics based data synthesis paradigm for artificial intelligence," *IEEE Signal Process. Mag.*, vol. 40, no. 2, pp. 129-140, 2023.
[39] Y. Zhou *et al.*, "CloudBrain-ReconAI: An online platform for MRI reconstruction and image quality evaluation," arXiv:2212.01878, 2022.
[40] Y. Zhou *et al*., "XCloud-pFISTA: A medical intelligence cloud for accelerated MRI," in *43rd Annual International Conference of the IEEE Engineering in Medicine and Biology Society (EMBC),* 2021, pp. 3289-3292.
[41] C. Qian *et al*., "Physics-informed deep diffusion MRI reconstruction: Break the bottleneck of training data in artificial intelligence," accepted by *20th IEEE International Symposium on Biomedical Imaging (ISBI)*, 2023.